

# CO<sub>2</sub> transport through swelling organic-rich nanoporous media: Insights on gas permeability from coarse-grained pore-scale simulations

Jian Wu<sup>a</sup>, Yixiang Gan<sup>a,b</sup>, Pengyu Huang<sup>c</sup>, Luming Shen<sup>a,\*</sup>

<sup>a</sup> School of Civil Engineering, The University of Sydney, NSW 2006, Australia

<sup>b</sup> Sydney Nano Institute, The University of Sydney, NSW 2006, Australia

<sup>c</sup> CSIRO Mineral Resources, QCAT, 1 Technology Court, Pullenvale, QLD, 4069, Australia

## ARTICLE INFO

Handling Editor: Jin-Kuk Kim

### Keywords:

CO<sub>2</sub> sequestration  
Adsorption  
Nanoporous media  
Gas transport  
Molecular dynamics

## ABSTRACT

Sorption-induced swelling reduces porosity and permeability in porous media, impacting long-term CO<sub>2</sub> storage injectivity. This study employs an innovative coarse-grained model to couple fluid flow with sorption-induced solid deformation at the pore-scale. Our model preserves the advantages of molecular dynamics in simulating complex fluid-solid interaction under nano-confinement while extending the time and length scales. Adjusting the gas-solid interaction energy controls solid swelling and gas slippage at pore walls. Gas permeability curves demonstrate a linear decline with the increasing gas-solid interaction energy in both swelling and non-swelling nanoporous media, with the former experiencing a greater drop. Surprisingly, in the regime of weak gas-solid interactions, swelling is not yet initiated and the porosity and permeability of flexible porous media increase, possibly due to gas flow-induced pore throat opening. Nanoporous media with lower initial porosity experience a greater permeability decline during swelling. The relationship between permeability and porosity changes shows a linear increase characterized by different slopes with varying initial porosities. These findings provide valuable insights into the complex interactions among gas transport, solid deformation, and porosity changes in nanoporous media, with implications for understanding and optimizing gas production and CO<sub>2</sub> storage in realistic geological environments.

## 1. Introduction

Many natural and synthetic porous materials, such as clays, organic matter, sponges, concrete, and hydrogel, exhibit the ability to swell upon fluid adsorption. Adsorption-induced deformation occurs when the adsorbing fluid exerts a pressure of hundreds of atmospheres on solid surfaces (Gor et al., 2017). In the presence of fluid, swelling may significantly reduce the pore channel size and constrain the flux through a network of channels, leading to a permeability decrease of the porous medium (Mo et al., 2022). In subsurface reservoirs, CO<sub>2</sub> injection plays an important role in enhancing natural gas recovery and achieving carbon storage. CO<sub>2</sub> induces swelling after entering the organic matrix, such as kerogen (Wu et al., 2022a), and closes the microfractures, reducing the porosity and permeability of the rock matrix. The evolution of permeability controls the transport and storage characteristics of CO<sub>2</sub>. Hence, sorption-induced swelling can eventually have an adverse impact on the long-term gas injectivity and storage capacity in organic-rich shale and coal (Cui et al., 2007). The response of

permeability to sorption-induced swelling is generally studied as a function of pore pressure (Sheng et al., 2019; Wang et al., 2012), and permeability reduction is found to be positively related to higher content of swelling agent and lower initial porosity (Aksu et al., 2015). Despite a great number of experimental and analytical work on permeability and swelling at continuum-scale, there is a lack of numerical studies revealing the fundamental effects of pore-scale geometric parameters on permeability and the permeability-porosity relations for swelling porous media, primarily due to the difficulty in boundary conditions to achieve full gas-solid coupling.

The fluid-solid coupling has been achieved by different numerical methods, including the smoothed particle hydrodynamics (SPH) (Bui and Nguyen, 2017; Feng et al., 2024; Mo et al., 2022; Shwetank et al., 2023), finite element method (FEM) (Jiang et al., 2018; Peters et al., 2023), lattice Boltzmann method (LBM) (Matias et al., 2021; Mou and Chen, 2021; Zhao et al., 2019), and discrete element method (DEM) (Hu et al., 2019; Sweijen et al., 2017). For example, Shwetank et al. (2023) coupled SPH and the finite difference method (FDM) to study fracturing

\* Corresponding author.

E-mail address: [luming.shen@sydney.edu.au](mailto:luming.shen@sydney.edu.au) (L. Shen).

<https://doi.org/10.1016/j.jclepro.2024.143253>

Received 9 June 2024; Received in revised form 14 July 2024; Accepted 23 July 2024

Available online 24 July 2024

0959-6526/© 2024 The Authors. Published by Elsevier Ltd. This is an open access article under the CC BY license (<http://creativecommons.org/licenses/by/4.0/>).

induced by fluid flow in a deformable porous medium, where SPH is used for solid deformations and fracture propagation and FDM for pore pressure. Peters et al. (2023) used FEM to study miscible multiphase transport in deformable porous media based on the theory of porous media (TPM). In their model, the fluid-solid interaction is realized in the balance equations through the effective stresses. To address the effect of swelling on fluid flow, Matias et al. (2021) used three types of nodes to represent fluid, solid, and interface in LBM, with the distribution functions of the fluid node set to zero during swelling. Mo et al. (2022) achieved swelling in the SPH by increasing the lengths of harmonic bonds connecting smaller particles composing the solid as a function of water concentration. Sweijen et al. (2017) extended DEM with an analytical solution defining the swelling rate by diffusion of local water concentration. However, these models operate at the macroscopic scale and primarily rely on derived equations to characterize the swelling behaviors rather than emerging directly from fluid-solid interactions at pore-scale, thus may not be able to capture the molecular details at interfaces. Moreover, they generally require significant modifications to simulate fluid in complex systems. For example, the basic LBM model cannot be directly used for nano-confined flow and needs extensive work in dealing with the movable boundary conditions in the case of solid deformation (Liu et al., 2021, 2023; Matias et al., 2021; Mou and Chen, 2021). Molecular dynamics (MD) is a powerful tool for studying the coupling between fluid flow and solid deformation due to the minimal effort in dealing with gas-solid interactions at boundaries. For example, Wu and Firoozabadi (2019) investigated methane transport through a deformable kerogen matrix and evaluated the effect of microstructural flexibility on gas transport. Wu et al. (2022b) constructed 2–4 nm slit nanochannels confined between kerogen matrix to study the reduced gas transport due to kerogen swelling. Furthermore, Simeski and Ihme (2023) used reactive molecular dynamics simulations to study the crack initiation of single-crystal quartz during CO<sub>2</sub> injection. However, MD simulations are limited in spatial and temporal domains due to the high computational costs.

Coarse-grained molecular dynamics (CGMD) bridges nano- and micro-scales by mapping a group of atoms/molecules into a single coarse-grained (CG) particle with reduced degrees of freedom in the system (Huang et al., 2018). Dissipative particle dynamics (DPD) is a coarse-graining simulation method using solely repulsive forces to describe hydrodynamic interactions (Español and Warren, 2017). It has shown successes in simulating saturated and unsaturated flow through porous media (Liu et al., 2007), heat conductivity, and mass diffusion (Zeng et al., 2021) usually in the absence of solid deformation. Many-body dissipative particle dynamics (MDPD) is a modified DPD model by turning the sign of the original repulsive term (i.e., becomes attractive) and adding a density-dependent repulsive term, which can be used to reproduce more complex equations of state (EOS) (Xia et al., 2017). Fluid-fluid interfaces can be tuned by changing the attractive interaction between the wetting and non-wetting phases (Xia et al., 2017). With MDPD, Chen et al. (2014) conducted a sensitivity study of the spontaneous capillary displacement between two fluids by varying parameters such as the fluid wetting property, miscibility, and capillary radius. Hulikal Chakrapani and den Otter (2020) studied the capillary imbibition of binary fluids in cylindrical pores. Liu and Brancio (2021) investigated single-phase fluid flow through nanoporous media of varied average pore sizes. Xia et al. (2022) simulated flooding in a micro block (957.5 nm × 952.5 nm × 945.0 nm) of a realistic shale sample saturated with a source fluid. Considering mechanical deformation under loading, Masoud and Alexeev (2010) developed a mesoscopic DPD model to study the permeation and diffusion through mechanically deformed random polymer networks. They found that permeability and diffusivity increase in the elongated direction but decrease in the transverse direction following a linear relationship.

Although sorption-induced solid swelling is not typically coupled in the CGMD framework of multiphase flow, the swelling behavior itself can be simulated in microgels that are often represented by a random

network of bead-spring chains immersed in an explicit solvent (Camerin et al., 2018; Nikolov et al., 2017). With coarse-grained simulations, the mechanics and swelling kinetics of solids can be widely adjusted to match theoretical calculations and experimental measurements solely based on fluid-solid interactions (Camerin et al., 2018; Nikolov et al., 2017). Using different interaction models for fluids and solids, we have coupled the solid swelling with single-phase flow within the CGMD framework. In this study, we adopt this novel CGMD model to perform pore-scale simulations of gas transport in complex pore networks. CO<sub>2</sub> adsorption can induce swelling of the nanoporous structure of rock matrix, which turns into a porosity decrease and constrains the mass flux passing through. The gas permeability in swelling organic-rich nanoporous media is compared with that in non-swelling nanoporous media. System parameters such as gas pressure, gas-solid affinity, swelling ratio, porosity, and pore size are evaluated to provide insights into the effect of sorption-induced swelling on permeability during CO<sub>2</sub> injection.

## 2. Computational methods

### 2.1. Formulation of the CGMD model

This work is intended to address gas permeability through swelling nanoporous media in the context of CO<sub>2</sub> sequestration. To maintain the amorphous and swelling nature of kerogen (i.e., the major organic-rich nanoporous material in shale and coal matrix), we use disordered bead-spring chain networks with the finite extensible nonlinear elastic (FENE) potential for solids, which is expressed as

$$E = -0.5KR_0^2 \ln \left[ 1 - \left( \frac{r}{R_0} \right)^2 \right] + 4\epsilon_s \left[ \left( \frac{\sigma_s}{r} \right)^{12} - \left( \frac{\sigma_s}{r} \right)^6 \right] + \epsilon_s, \quad (1)$$

where  $K$  is the bond stiffness,  $R_0$  is the maximum extended bond length,  $r$  is the distance between two particles, and  $\epsilon_s$  and  $\sigma_s$  are the Lennard-Jones (LJ) energy minimum and distance. The second LJ term is repulsive only with a cut-off at  $2^{1/6}\sigma_s$ , which is the location of the LJ potential minimum. A short-range 12-6 LJ non-bonding potential truncated at  $2.5\sigma_s$  is used between particles that are not directly bonded. A total of 500 chains are randomly placed into a simulation box to form the soft solid structure, each containing 20 solid CG particles with a per-particle mass of  $1.24 \times 10^{-20}$  kg. The solid structure is flexible and can deform when stresses are imposed by gas particles upon adsorption. Moreover, the position of the solid structure is constrained in the center of the simulation box by adding a self-tethering spring with a small force constant at  $K_s^* = 10$  onto each CG solid particle. In contrast, increasing the self-tethering force constant to  $K_s^* = 10,000$  can make the solid structure fully rigid and non-deformable.

The CO<sub>2</sub> gas phase is characterized by the DPD model, which comprises a conservative force  $F^C$ , a dissipative force  $F^D$ , and a random force  $F^R$  (Groot and Warren, 1997). Here, the non-conservative parts  $F^D$  and  $F^R$  are replaced by the Nosé-Hoover thermostat for simultaneous control of the gas-solid system (Huang et al., 2018, 2020)

$$\mathbf{F} = (F^C + F^D + F^R) \mathbf{e}_{ij}, \quad (2)$$

$$F^C = Aw(r), \quad (3)$$

$$F^D = F^R = 0, \quad (4)$$

$$w(r) = 1 - \frac{r}{r_c}, \quad (5)$$

where  $\mathbf{e}_{ij}$  is the unit vector in the direction  $\mathbf{r}_i - \mathbf{r}_j$ ,  $w(r)$  is the weight function varying between 0 and 1, and  $r_c$  is the pairwise cut-off. Each gas particle has a mass of  $2.07 \times 10^{-21}$  kg, about the size of 28 actual CO<sub>2</sub> molecules.

Gas-solid interactions are modeled by the short-range LJ potential. Solid swelling induced from gas adsorption is controlled through the energy well depth  $\varepsilon_{gs}$  and the distance  $\sigma_{gs}$  of the LJ potential function. The cut-off distance is set as  $2.5 \sigma_{gs}$ , beyond which the gas-solid interaction goes to zero. More details about the development of this novel CGMD model, along with calibration and validation cases of gas transport in swelling porous media, can be found in our previous work (Wu et al., 2024). To recover the fluid properties of CO<sub>2</sub> and the swelling ratio of solid, we set

$$\begin{cases} K^* = 9000, R_0^* = 2, \varepsilon_s^* = 30, \sigma_s^* = 0.6 \\ A^* = 44.1, r_c^* = 0.63 \\ \varepsilon_{gs}^* = 1 - 8, \sigma_{gs}^* = 0.5 \end{cases}$$

## 2.2. Simulation details

The complex porous structures can be created from the solid phase in a few steps. Firstly, 500 bead-spring chains are randomly distributed into a large simulation box ( $1 \mu\text{m} \times 1 \mu\text{m} \times 1 \mu\text{m}$ ) with the chain tool in LAMMPS (Thompson et al., 2022), ensuring no particle overlapping. The simulation box is then relaxed in the NPT ensemble under atmospheric conditions, which reduces gap spaces between chains and increases the solid density. The condensed solid ( $0.45 \mu\text{m} \times 0.45 \mu\text{m} \times 0.45 \mu\text{m}$ ) has an equilibrium density similar to kerogen of  $1249 \text{ kg/m}^3$  and a Young's modulus of 0.8 GPa. To increase the domain size of the porous medium, the simulation box is replicated  $2 \times 2$  in the x and z directions ( $0.9 \mu\text{m} \times 0.45 \mu\text{m} \times 0.9 \mu\text{m}$ ). SEM images indicate that the pore bodies in organic matter are usually spherical (Zhang et al., 2020). The selected pore sizes are representative in deep marine shales (Meng et al., 2022), which have abundant organic nanopores ranging from 57 to 109 nm. These macropores can act as the primary transport and storage sites for gas. Thus, we have randomly generated a number of spherical pores within the simulation box containing the solid to create organic nanoporous media with different porosities (S1, S2, S3 and S4). Moreover, two additional samples (b and c) with altered porous structures have also been created under each porosity. This is done by deleting spherical regions with pre-set radii from the solid phase in a random manner, followed by a new cycle of relaxation at 333.15 K to ensure no further structural change. The porous media can be visualized using OVITO (Stukowski, 2009) with porosity being calculated, as illustrated in Fig. 1. The final region of interest (ROI) has a dimension of  $1 \mu\text{m} \times 0.45 \mu\text{m} \times 0.9 \mu\text{m}$ , consisting of  $\sim 25,000$  solid CG particles. S1, S2, S3, and S4 have increasing porosities at 0.33, 0.39, 0.45, and 0.51 but the similar pore size distribution with the pore radius ranging from 35.4 nm to 106.2 nm.

Gas reservoirs are placed at the right and left sides of the ROI. The

initial distributions of CG gas particles are created on the simple cubic (SC) lattice points inside the regions of the gas reservoirs as shown in Fig. 1. Two pistons are used to control the pressure within the gas reservoirs, and gas flow is generated in the x-direction when there is a pressure difference of 2.5 MPa between the two gas reservoirs. After the simulation is started, the gas particles first saturate the ROI from two sides. The gas pressure of the two reservoirs, the average gas velocity within the ROI, and the gas particle numbers in the reservoirs and ROI are monitored during the simulation. Eventually, the two pistons can move from left to right at a constant velocity as these values stabilize over time. The gas transport data is then produced at this time from a total of 500,000 to 1,000,000 timesteps with a sampling frequency of every 10 timesteps. The simulation is typically ceased before the left piston reaches the ROI under the current setup. Otherwise specified, the average gas pressure between the two gas reservoirs is kept at 15 MPa by the pistons to achieve a higher ratio of sorption-induced swelling. The DPD model recovers the CO<sub>2</sub> density at  $602 \text{ kg/m}^3$  and viscosity at  $40.4 \mu\text{Pa s}$ , respectively (NIST: density  $604.1 \text{ kg/m}^3$ , viscosity  $45.9 \mu\text{Pa s}$  (Linstrom and Mallard, 2022)). It is noted that a reduction factor of 0.2 is used to convert the dimensionless time to the physical time in order to match the simulated and reported viscosities (Huang et al., 2020).

A total of 102 simulation cases have been performed in 12 nanoporous structures. All simulations are performed with LAMMPS at a typical reservoir temperature  $T = 333.15 \text{ K}$  using the velocity-Verlet algorithm to integrate the equations of motion with a timestep of 25.7 fs. Setting the fundamental unit quantities for mass, energy, and distance as  $M = 7.29 \times 10^{-21} \text{ kg}$ ,  $E = 5.53 \times 10^{-18} \text{ J}$ , and  $D = 3.54 \times 10^{-8} \text{ m}$ , all physical properties can be mapped into the dimensionless system (indicated by \*).

## 3. Results and discussion

### 3.1. Permeability dependence on pressure

As described in Section 2.2, gas starts to saturate the porous medium when the simulation initiates. After gas transport has reached a steady state in the system, permeability is calculated based on the number of CG gas particles passing through the ROI versus time according to the Darcy's law

$$K = \frac{Q\mu}{\rho A \nabla P}, \quad (6)$$

where  $Q$  is the mass flux,  $\mu$  is the viscosity,  $\rho$  is the gas density,  $A$  is the cross-sectional area normal to the flow direction, and  $\nabla P$  is the pressure

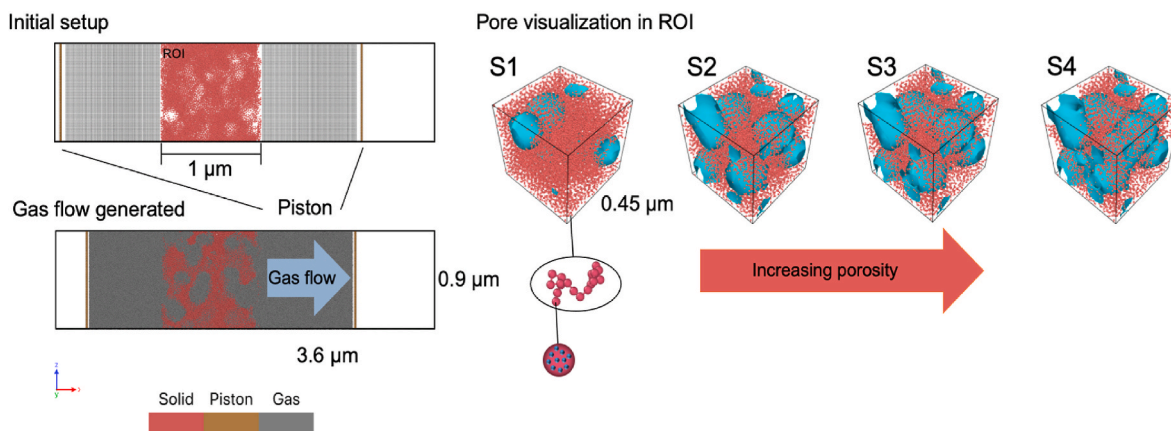


**Fig. 1.** Illustration of gas transport through a nanoporous medium. Pressure is controlled by pistons placed at two sides of the gas reservoirs. The solid structure is constructed by 500 bead-spring chains, with each CG particle representing a group of real atoms/molecules. Porosity increases from S1 to S4. Spherical pore bodies are visualized and highlighted in cyan. Periodic boundary conditions are applied in all directions. (For interpretation of the references to colour in this figure legend, the reader is referred to the Web version of this article.)

gradient. Darcy's law is still valid since viscous flow dominates in nanoporous media when gas pressure is 15 MPa and Reynolds number is lower than 1–10. Our previous work also validated the permeability calculated from Darcy's law with the Kozeny-Carman equation in a simple porous medium of spherical particles whose porosity and solid diameters are known (Wu et al., 2024). As shown in Fig. 2a, the permeability increases with the porosity increasing from S1 to S4. It is found that higher gas pressure reduces the permeability in all the four cases because sorption-induced swelling is positively related to gas pressure, which decreases the pore spaces available for gas transport. In Fig. 2b, the gas-solid LJ interaction energy is varied for S1, which induces both gas slippage ( $\epsilon_{gs}^* = 1$ ) and swelling ( $\epsilon_{gs}^* = 5.7$  and 6.2). When the gas pressure is 15 MPa, the nominal swelling ratios resulting from  $\epsilon_{gs}^* = 1$ ,  $\epsilon_{gs}^* = 5.7$ , and  $\epsilon_{gs}^* = 6.2$  are 0%, 5.4%, and 12.5%, respectively, as measured from a spherical solid particle immersed in gas. The S1 permeability at  $\epsilon_{gs}^* = 1$  is found over twice higher than the rest cases, which is attributed to the gas slippage effect arising from the reduced gas affinity at pore walls as evidenced by our previous study on nanochannel flow (Wu et al., 2024). At  $\epsilon_{gs}^* = 5.7$  and  $\epsilon_{gs}^* = 6.2$ , gas slippage becomes relatively negligible due to the strong gas affinity at pore walls, and swelling takes control and leads to the permeability decrease with the increasing  $\epsilon_{gs}^*$ . Moreover, permeability is more sensitive to  $\epsilon_{gs}^*$  as the gas pressure increases, mostly owing to the positive correlation between sorption-induced swelling and pressure (Wu et al., 2022a).

### 3.2. Comparison between swelling and non-swelling porous media

Gas permeability through S1, S2, S3, and S4 is plotted as a function of the gas-solid interaction energy  $\epsilon_{gs}^*$ , which varies from 1 to 8. A comparison is made between permeabilities in the non-swelling and swelling nanoporous media. As shown in Fig. 3, permeability decreases linearly with the increasing gas-solid interaction energy in both cases. However, a faster permeability decrease is seen when swelling is allowed within the solid structure, attributed to the narrowed flow pathway through pore spaces. Although the available pore spaces always remain the same in the non-swelling porous media, the increased gas-solid interaction energy leads to higher gas affinity onto the pore walls, which retards the gas mass flux passing through. Consequently, two separate effects can slow down the gas transport when increasing the gas-solid interaction energy in swelling porous media – reduced pore spaces and higher affinity at pore walls, while the first effect dominates over the second one.

Another interesting observation is that there is a crossover point around  $\epsilon_{gs}^* = 4 - 6$  for permeability curves between the non-swelling and swelling porous media. Below this crossover point, the permeability in the swelling porous media is higher than that in the non-swelling one, and vice versa. This enhancement may be attributed to the flexibility of the porous solid structure. Wu and Firoozabadi (2019)

found that pore throats can occasionally open in flexible kerogen microstructures and provide additional flux. When the gas-solid interaction energy is low, swelling does not occur, and the gas affinity onto pore walls is also minimal, which leads to gas slippage (this case usually occurs at low gas pressure in real life). As swelling gradually takes over, the additional gas flux from the pore throat opening becomes negligible compared with the contracted main flow pathways. The difference between permeabilities in swelling and non-swelling porous media increases significantly as the swelling ratio of the solid structure increases.

Fig. 4a shows the decrease in pore volume (denoted as porosity  $n$ ) as swelling is increased by increasing  $\epsilon_{gs}^*$ . It can be seen that many pore spaces have been occluded at high swelling ratios. In Fig. 4b, the solid swelling ratio is measured as a function of  $\epsilon_{gs}^*$  by immersing a spherical solid into gas, which can be fitted by a sigmoid function. Based on the swelling ratio, the porosity change can be easily calculated with the initial porosity ranging between 0.35 and 0.6. The calculation generally agrees well with the simulated data (i.e., porosity measurements of swollen porous structures). However, deviations become apparent as porosity increases by up to 20% when  $\epsilon_{gs}^* < \sim 5$  (the swelling ratio is  $\sim 0$ ), aligning with our previous discussion on pore throat opening due to the microstructure flexibility.

By calculating the relative permeability difference between the swelling and non-swelling porous media at the same gas-solid interaction energy, the permeability reduction resulting from swelling is plotted as a function of the swelling ratio, as shown in Fig. 4c. With the increase of the swelling ratio, the permeability reduction increases and generally follows a near-linear relationship. These four curves are approximately parallel to each other before reaching the limit at 100% permeability reduction. In the porous media with lower porosities, S1 and S2, all the available gas flow pathways are restricted when the swelling has reached  $\sim 40\%$ , which is signified by a permeability reduction of  $\sim 100\%$ . On the contrary, the permeability remains nearly unchanged in highly porous structures such as S3 and S4 when the swelling is insignificant. It is noted that the permeability in S4 has even slightly increased at  $\sim 5.4\%$  of swelling, which may be attributed to the structure flexibility causing pore throat opening by gas flow. In summary, it can be inferred that a higher relative permeability difference is likely expected in nanoporous media with lower porosities, regardless of the swelling ratio. In low-porosity porous media, the pore network usually has a poor connection with fewer flow pathways. Swelling of the nanoporous structure can cause a greater proportional change of porosity and easily block these few pathways, reducing the permeability significantly. High-porosity porous media, however, may still have many alternative flow pathways available after swelling. Hence, their permeability is less sensitive to swelling. Based on the MD studies, CO<sub>2</sub> sorption-induced kerogen swelling is typically less than 10% (Ho et al., 2018). However, the results herein indicate that 10% of swelling may still greatly affect the permeability of CO<sub>2</sub> in shale characterized by a low porosity during the injection process, reducing the injectivity as

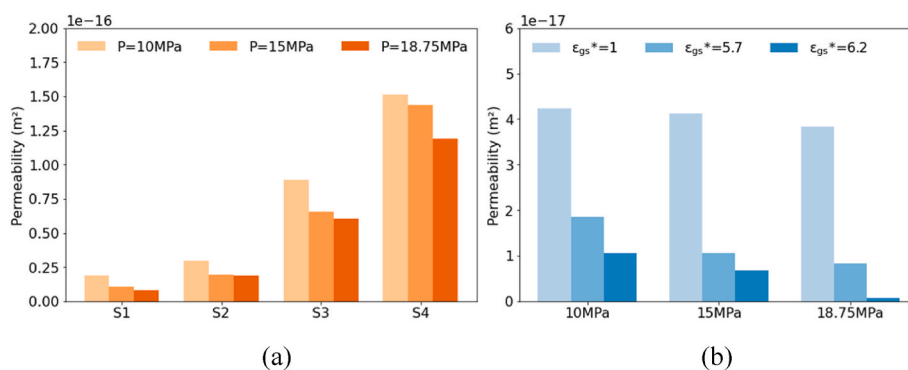


Fig. 2. (a) Permeability in S1, S2, S3 and S4 under the gas pressure of 10 MPa, 15 MPa and 18.75 MPa at  $\epsilon_{gs}^* = 5.7$ . (b) Permeability in S1 under the gas pressure of 10 MPa, 15 MPa and 18.75 MPa with varying  $\epsilon_{gs}^*$  from 1 to 6.2.

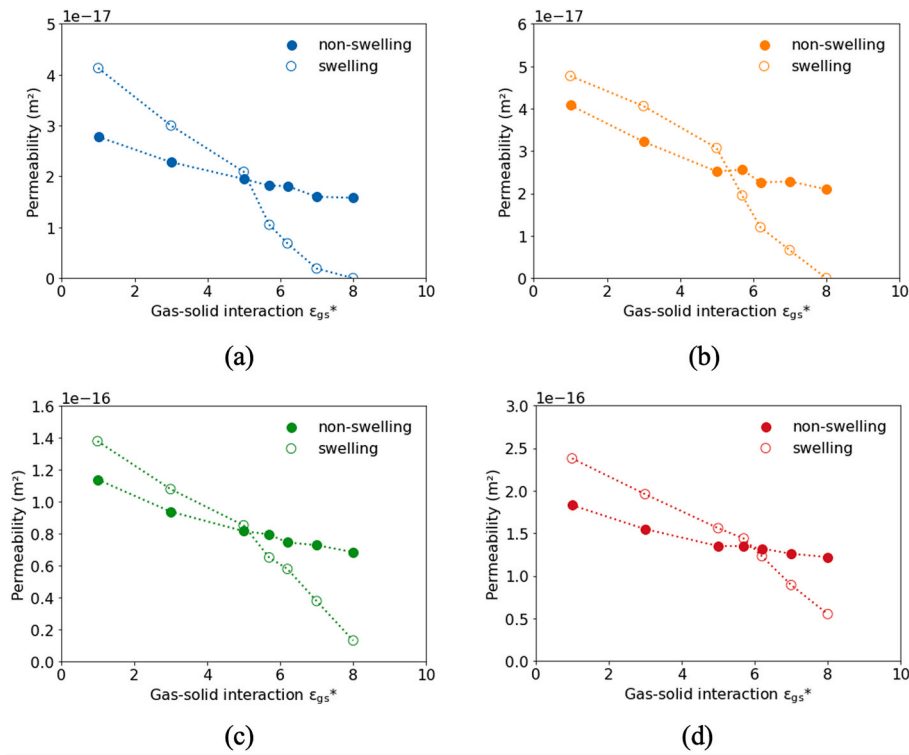


Fig. 3. Comparison between permeabilities in swelling and non-swelling nanoporous media as the gas-solid interaction energy  $\epsilon_{gs}^*$  changes. The initial porosities of (a) S1 (b) S2 (c) S3 and (d) S4 are 0.33, 0.39, 0.45, and 0.51, respectively.

time evolves.

### 3.3. Permeability as a function of porosity

The permeability dependence on porosity is illustrated in Fig. 5. In the non-swelling porous media, changing the gas-solid interaction energy between 5.7 and 8 leads to minor permeability variations in S1, S2, S3, and S4 (Fig. 5a). The Kozeny-Carman equation  $k = Cn^3 / (1 - n)^2$ , where  $C$  is related to the solid structure and treated as a fitting parameter, is used to fit the permeability data as a function of porosity  $n$ , as shown in Fig. 4a. A good match can be obtained when the fitting parameter is set as  $2.3 \times 10^{-16} \text{ m}^2$ , validating the results of gas transport simulated by the CGMD model. This also further suggests that the elevated gas-solid affinity within this range has limited effects on the gas transport through the porous media with relatively small permeability reductions as shown in Fig. 3.

When swelling is enabled, the relationship between permeability and porosity becomes dependent on the structure of the porous media as S1, S2, S3, and S4 manifest different permeability curves with respect to porosity, as shown in Fig. 5b. As swelling increases, the porosity decreases, and the available gas flow pathways reduce. Permeability changes show a linear relationship with porosity variations in the swelling porous media (Fig. 5c), but different slopes are found for S1, S2, S3, and S4. Based on Fig. 5b, it can be seen that the slope ( $7.17 \times 10^{-17} \text{ m}^2$ ,  $1.17 \times 10^{-16} \text{ m}^2$ ,  $3.68 \times 10^{-16} \text{ m}^2$ ,  $6.83 \times 10^{-16} \text{ m}^2$ ) increases with the initial porosity (0.33, 0.39, 0.45, 0.51) of the swelling porous media and is the highest in S4. This suggests that different gas permeabilities can arise at the same porosity, and porosity is not the sole predictor of permeability in swelling porous media. These findings are consistent with the study by Hommel et al. (2018), which suggests that the quantitative relationship between porosity and permeability is influenced by the morphology of the pore space. When significant alterations occur in the porous structure, it is necessary to consider other representative elementary volume (REV)-scale parameters related to pore geometry, such as specific surface area and tortuosity, in the permeability-porosity

relationship. Based on gas transport through porous media composed of spherical particles, a modified Kozeny-Carman equation has been previously developed to include the swelling effect (Wu et al., 2024).

$$K = \frac{d_{p0}^2 n^3}{36\kappa(1 - n)^{4/3}(1 - n_0)^{2/3}}, \tag{7}$$

where  $d_{p0}$  is the initial diameter of the spherical solids,  $n_0$  is the initial porosity, and  $\kappa$  is the Kozeny constant. It can be seen that permeability is positively related to  $n_0$ . Moreover,  $\kappa$ , which accounts for the geometry of the porous media, may also change differently regarding the initial pore structure during swelling. These effects can contribute to the deviations observed between Fig. 5a and b.

### 3.4. Effect of pore size

The effect of pore size is analyzed by generating two additional porous sub-structures (b and c) to S1, S2, S3, and S4 (non-uniform pore size distribution at 35.4–106.2 nm) with the porosity controlled. Sub-structures b and c have a uniform pore size at 70.8 nm and 106.2 nm, respectively. Fig. 6 shows the dependence of permeability on porosity with varying pore sizes. Although the initial porosity is designed to be the same, it is not feasible to control the porosities of these porous structures after relaxing and swelling, which are used for the data plotting here. Thus, slight deviations are seen in porosity among sub-structures. With similar porosity, sub-structure c manifests the highest permeability in S2, S3, and S4, while sub-structure b has the lowest in S3 and S4. The permeability increases with the increasing pore size in S3 and S4, but S1 and S2 show a different pattern. The underlying reason could be attributed to variations in pore connectivity. A higher porosity tends to facilitate a greater likelihood of interconnected flow pathways within the porous medium. Conversely, a lower porosity may result in insufficient pore connectivity, impeding the formation of continuous flow pathways across the porous medium. Even with a larger pore size, S1 and S2 may have a poorer pore connectivity than that with a smaller

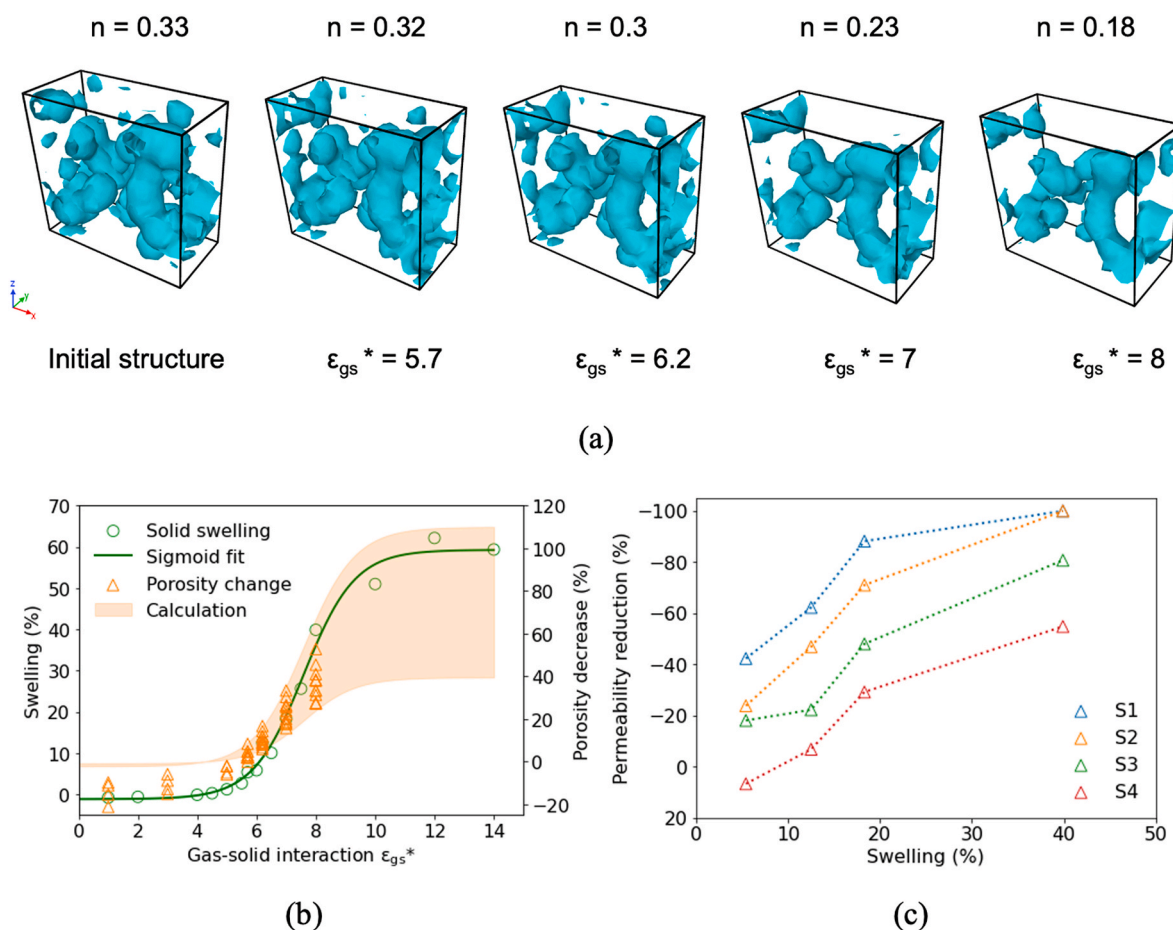


**Fig. 4.** (a) Visualization of pore volume evolution as the gas-solid interaction energy increases swelling in S1. (b) Swelling (left y-axis) and porosity decrease (right y-axis, porosity measurements from sub-structures in Section 3.4 are also included) as a function of the gas-solid interaction energy for S1, S2, S3 and S4. The swelling curve of a solid sphere follows a sigmoid relationship with  $\epsilon_{gs}^*$ . The orange-shaded area shows the calculated porosity change from swelling with the upper limit at an initial porosity of 0.35 and the lower at 0.6. (c) Permeability reduction as a function of the nominal swelling ratio as in Fig. 4b for S1, S2, S3, and S4, calculated from the relative permeability difference between the swelling and non-swelling nanoporous media. (For interpretation of the references to colour in this figure legend, the reader is referred to the Web version of this article.)

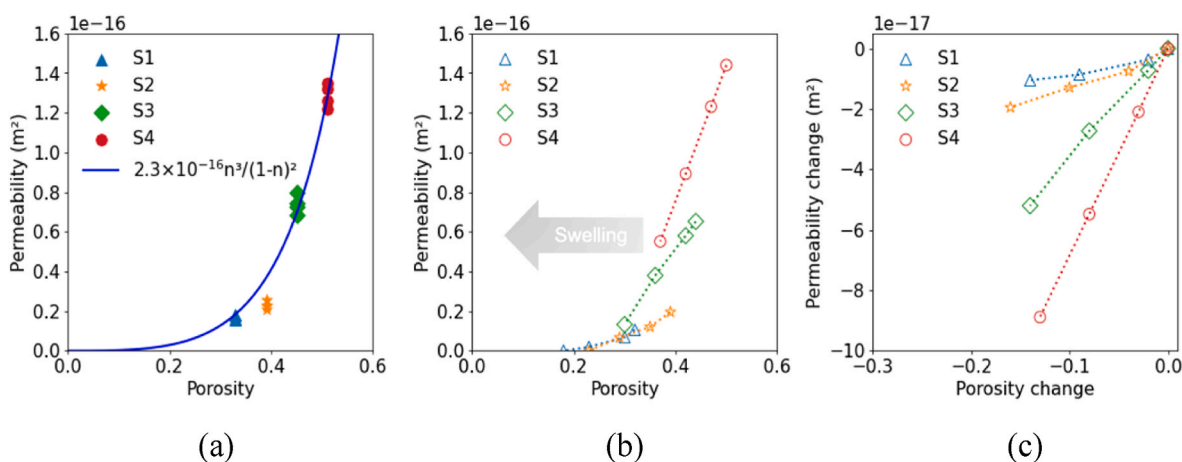


**Fig. 5.** Permeability dependence on porosity with varying gas-solid interaction energies in S1, S2, S3, and S4 (a) in the absence of solid swelling versus (b) in the presence of solid swelling. The gas-solid interaction energy  $\epsilon_{gs}^*$  ranges between 5.7 and 8. (c) Permeability change as a function of porosity variation in the swelling porous media.

pore size when the porosity is fixed.

In S1 and S2, the permeability changes with porosity at different gradients as the pore size varies. The structure with the lowest initial

porosity, S1, also shows more non-linearity. In comparison, the three lines in S3 and S4 are linear and parallel, indicating a similar changing trend of the permeability when swelling occurs. This observation

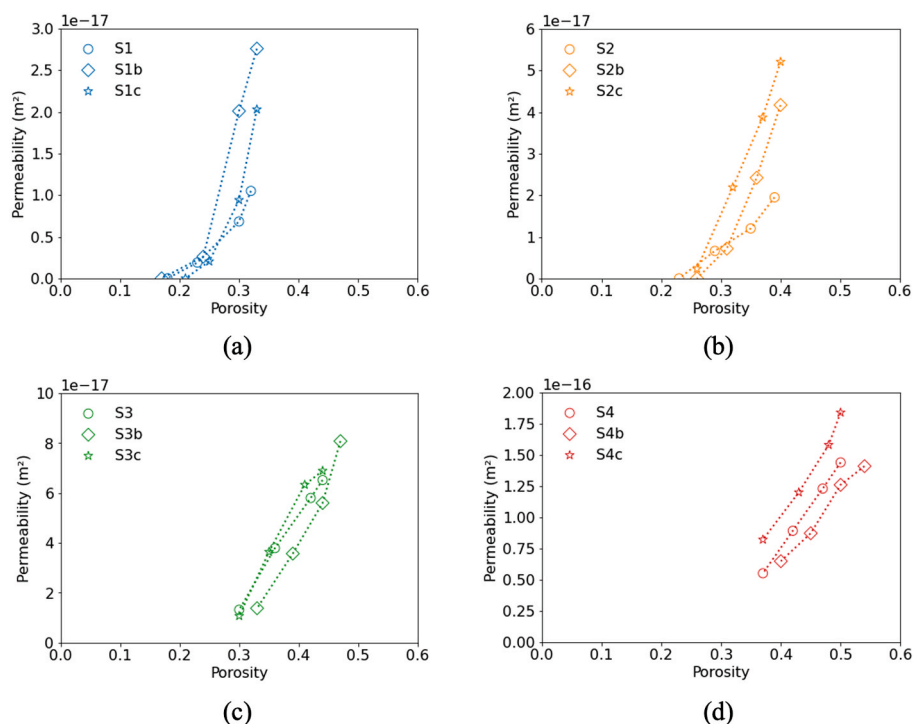


**Fig. 6.** Permeability dependence on porosity with varying pore sizes. S1, S2, S3, and S4 have a pore size distribution between 35.4 nm and 106.2 nm. Letters “b” and “c” denote sub-structures of S1, S2, S3, and S4 with a uniform pore size of 70.8 nm and 106.2 nm, respectively.

suggests that the permeability evolution curve in swelling porous media may be less sensitive to the porous structure if the initial porosity is large.

Permeability reduction is one of the common technical difficulties encountered in field projects of CO<sub>2</sub> geological storage. It is expected to maintain a high injectivity of CO<sub>2</sub> long enough for better storage outcomes. These findings suggest that low-porosity shale can be very sensitive to swelling, with gas injectivity likely to reduce to zero. One should select a site with a more porous rock matrix to avoid the complete blockage of flow pathways by sorption-induced swelling. In large-scale modeling, permeability is the most important parameter used to represent the resistance to fluid flow in the porous medium on the REV-scale (Hommel et al., 2018). Our results show that swelling has a great impact on gas permeability. The permeability-porosity relation for swelling porous media can differ from that for non-swelling porous media. As continuum-scale simulation models commonly adopt the Kozeny-Carman equation to describe permeability as a function of porosity, a precise porosity-permeability relation needs to be developed at the continuum level to accurately predict permeability reduction and CO<sub>2</sub> storage capacity in organic-rich nanoporous media. This can possibly be achieved by further modifying Eq. (7) for irregular solid matrix and correlating the geometrical parameters to the swelling ratio. Moreover, special care should be given to a critical porosity at which the porous structure becomes impermeable (i.e., 100% permeability reduction) due to swelling.

#### 4. Conclusions

Gas adsorption-induced swelling can close the pore spaces of the organic-rich matrix, significantly reducing long-term gas injectivity and storage capacity during CO<sub>2</sub> geological sequestration. To understand the permeability evolution in swelling porous media, a novel coarse-graining model for coupling microscale fluid flow with solid deformation has been employed. This study focuses on the effect of swelling on CO<sub>2</sub> transport through complex pore networks within organic matter. The main conclusions are.

- Permeability becomes increasingly responsive to the gas-solid interaction energy at elevated gas pressures, primarily due to the higher induced swelling ratios.
- The gas permeability curves exhibit a proportional decline with the increasing gas-solid interaction in both swelling and non-swelling porous media. This phenomenon is primarily associated with solid swelling and gas-solid affinity, respectively. Notably, the impact of solid swelling on permeability is significantly more pronounced than that of gas-solid affinity. A crossover point at  $\epsilon_{gs}^* \sim 5$  is found between the two permeability curves, below which the permeability in the swelling porous media surpasses that in the non-swelling one.
- Nanoporous media with a lower initial porosity exhibit higher ratios of porosity decrease and permeability reduction during swelling. Although the decreased porosity can be generally calculated from the swelling ratio, it is noteworthy that an increase is found when the gas-solid interaction is weak ( $\epsilon_{gs}^* < \sim 5$ ).
- In non-swelling porous media, permeability follows the Kozeny-Carman equation. However, permeability becomes dependent on the initial porosity in swelling porous media, revealing a linear increase with porosity characterized by different slopes. Additionally, the permeability-porosity correlation is also influenced by the pore size.

These results imply that sorption-induced swelling, generally arising with increasing gas pressure, plays a vital role in reducing permeability. In contrast, permeability can be slightly enhanced at low pressure (i.e., weak gas-solid interaction) due to the flexibility of the porous structure. The commonly applied porosity-permeability relation may not be sufficient for the swelling porous media. Large-scale models can fail to accurately predict the CO<sub>2</sub> storage capacity without considering the dynamic permeability evolution from sorption-induced swelling. Future studies are recommended to understand the pore structure change during swelling and consider the effect of moisture content. The addition of water will lead to a two-phase flow problem, which requires further calibration of water static and dynamic properties, interfacial tension, contact angle, etc.

## CRedit authorship contribution statement

**Jian Wu:** Writing – original draft, Visualization, Validation, Methodology, Investigation, Formal analysis, Data curation, Conceptualization. **Yixiang Gan:** Writing – review & editing, Supervision, Investigation. **Pengyu Huang:** Writing – review & editing, Methodology, Investigation. **Luming Shen:** Writing – review & editing, Supervision, Resources, Project administration, Investigation.

## Declaration of competing interest

The authors declare that they have no known competing financial interests or personal relationships that could have appeared to influence the work reported in this paper.

## Data availability

Data will be made available on request.

## Acknowledgments

This work was supported in part by the Australian Research Council through Discovery Projects Scheme (DP200101919), the Faculty of Engineering of the University of Sydney through the Career Advancement Award and the Office of Global and Research Engagement at the University of Sydney through University of Sydney – Zhejiang University Ignition Grants. The authors acknowledge the use of the National Computational Infrastructure (NCI) which is supported by the Australian Government, and accessed through the Sydney Informatics Hub HPC Allocation Scheme, which is supported by the Deputy Vice-Chancellor (Research), University of Sydney.

## References

- Aksu, I., Bazilevskaia, E., Karpyn, Z., 2015. Swelling of clay minerals in unconsolidated porous media and its impact on permeability. *GeoResJ* 7, 1–13.
- Bui, H.H., Nguyen, G.D., 2017. A coupled fluid-solid SPH approach to modelling flow through deformable porous media. *Int. J. Solid Struct.* 125, 244–264.
- Camerin, F., Gnan, N., Rovigatti, L., Zaccarelli, E., 2018. Modelling realistic microgels in an explicit solvent. *Sci. Rep.* 8 (1), 14426.
- Chen, C., Lu, K.J., Li, X.F., Dong, J.F., Lu, J.T., Zhuang, L., 2014. A many-body dissipative particle dynamics study of fluid-fluid spontaneous capillary displacement. *RSC Adv.* 4 (13), 6545–6555.
- Cui, X.J., Bustin, R.M., Chikatararla, L., 2007. Adsorption-induced coal swelling and stress: implications for methane production and acid gas sequestration into coal seams. *J. Geophys. Res. Solid Earth* 112 (B10).
- Español, P., Warren, P.B., 2017. Perspective: dissipative particle dynamics. *J. Chem. Phys.* 146 (15), 150901.
- Feng, R., Fourtakas, G., Rogers, B.D., Lombardi, D., 2024. A general smoothed particle hydrodynamics (SPH) formulation for coupled liquid flow and solid deformation in porous media. *Comput. Methods Appl. Mech. Eng.* 419, 116581.
- Gor, G.Y., Huber, P., Bernstein, N., 2017. Adsorption-induced deformation of nanoporous materials-A review. *Appl. Phys. Rev.* 4 (1), 011303.
- Groot, R.D., Warren, P.B., 1997. Dissipative particle dynamics: bridging the gap between atomistic and mesoscopic simulation. *J. Chem. Phys.* 107 (11), 4423–4435.
- Ho, T.A., Wang, Y., Criscenti, L.J., 2018. Chemo-mechanical coupling in kerogen gas adsorption/desorption. *Phys. Chem. Chem. Phys.* 20 (18), 12390–12395.
- Hommel, J., Coltman, E., Class, H., 2018. Porosity-permeability relations for evolving pore space: a review with a focus on (Bio-)geochemically altered porous media. *Transport Porous Media* 124 (2), 589–629.
- Hu, Z., Zhang, Y., Yang, Z., 2019. Suffusion-induced deformation and microstructural change of granular soils: a coupled CFD–DEM study. *Acta Geotechnica* 14, 795–814.
- Huang, P., Shen, L., Gan, Y., Nguyen, G.D., El-Zein, A., Maggi, F., 2018. Coarse-grained modeling of multiphase interactions at microscale. *J. Chem. Phys.* 149 (12), 124505.
- Huang, P.Y., Shen, L.M., Gan, Y.X., Maggi, F., El-Zein, A., 2020. Numerical investigation of microscale dynamic contact angles of the CO<sub>2</sub>-water-silica system using coarse-grained molecular approach. *Comput. Mech.* 66 (3), 707–722.
- Hulikal Chakrapani, T., den Otter, W.K., 2020. Capillary imbibition of binary fluid mixtures in nanochannels. *Langmuir* 36 (42), 12712–12722.
- Jiang, C., Yao, J.-Y., Zhang, Z.-Q., Gao, G.-J., Liu, G., 2018. A sharp-interface immersed smoothed finite element method for interactions between incompressible flows and large deformation solids. *Comput. Methods Appl. Mech. Eng.* 340, 24–53.
- Linstrom, P., Mallard, W., 2022. NIST Chemistry WebBook, NIST Standard Reference Database Number 69. National Institute of Standards and Technology, Gaithersburg MD, 20899.
- Liu, C., Brancio, P.S., 2021. Pore size dependence of permeability in bicontinuous nanoporous media. *Langmuir* 37 (51), 14866–14877.
- Liu, L., Zhao, Y., Luo, M., Zhang, L., Aryana, S.A., 2023. Bridging adsorption behavior of confined CH<sub>4</sub>-CO<sub>2</sub> binary mixtures across scales. *Fuel* 354, 129310.
- Liu, L.F., Wang, Y.H., Aryana, S.A., 2021. Insights into scale translation of methane transport in nanopores. *J. Nat. Gas Sci. Eng.* 96, 104220.
- Liu, M., Meakin, P., Huang, H., 2007. Dissipative particle dynamics simulation of pore-scale multiphase fluid flow. *Water Resour. Res.* 43, W04411.
- Masoud, H., Alexeev, A., 2010. Permeability and diffusion through mechanically deformed random polymer networks. *Macromolecules* 43 (23), 10117–10122.
- Matias, A.F.V., Coelho, R.C.V., Andrade, J.S., Araujo, N.A.M., 2021. Flow through time-evolving porous media: swelling and erosion. *J. Comput. Sci-Neth* 53, 101360.
- Meng, M., Ge, H., Shen, Y., Ji, W., Li, Z., 2022. Insight into water occurrence and pore size distribution by nuclear magnetic resonance in marine shale reservoirs, southern China. *Energy Fuel* 37 (1), 319–327.
- Mo, C.J., Navarini, L., Liverani, F.S., Ellero, M., 2022. Modeling swelling effects during coffee extraction with smoothed particle hydrodynamics. *Phys. Fluids* 34 (4), 043104.
- Mou, X.Z., Chen, Z.Q., 2021. Pore-scale simulation of fluid flow through deformable porous media using immersed boundary coupled lattice Boltzmann method. *Transport Porous Media* 140 (3), 743–762.
- Nikolov, S., Fernandez-Nieves, A., Alexeev, A., 2017. Mesoscale modeling of microgel mechanics and kinetics through the swelling transition. *Appl. Math. Mech.* 39 (1), 47–62.
- Peters, S., Heider, Y., Markert, B., 2023. Numerical simulation of miscible multiphase flow and fluid–fluid interaction in deformable porous media. *Proc. Appl. Math. Mech.* 23 (2), e202300209.
- Sheng, G.L., Javadpour, F., Su, Y.L., 2019. Dynamic porosity and apparent permeability in porous organic matter of shale gas reservoirs. *Fuel* 251, 341–351.
- Shwetank, K., Deb, D., Pramanik, R., 2023. Development of coupled SPH-FDM numerical procedures for simulating the flow of fluid through deformable porous media. In: ARMA US Rock Mechanics/Geomechanics Symposium. ARMA. ARMA-2023-0118.
- Simeski, F., Ihme, M., 2023. Corrosive influence of carbon dioxide on crack initiation in quartz: comparison with liquid water and vacuum environments. *J. Geophys. Res. Solid Earth* 128 (1), e2022JB025624.
- Stukowski, A., 2009. Visualization and analysis of atomistic simulation data with OVITO—the Open Visualization Tool. *Model. Simulat. Mater. Sci. Eng.* 18 (1), 015012.
- Sweijen, T., Chareyre, B., Hassanizadeh, S.M., Karadimitriou, N.K., 2017. Grain-scale modelling of swelling granular materials: application to super absorbent polymers. *Powder Technol.* 318, 411–422.
- Thompson, A.P., Aktulga, H.M., Berger, R., Bolintineanu, D.S., Brown, W.M., Crozier, P.S., in 't Veld, P.J.J., Kohlmeyer, A., Moore, S.G., Nguyen, T.D., Shan, R., Stevens, M.J., Tranchida, J., Trit, C., Plimpton, S.J., 2022. LAMMPS—a flexible simulation tool for particle-based materials modeling at the atomic, meso, and continuum scales. *Comput. Phys. Commun.* 271, 108171.
- Wang, S.G., Elsworth, D., Liu, J.S., 2012. A mechanistic model for permeability evolution in fractured sorbing media. *J. Geophys. Res. Solid Earth* 117, B06205.
- Wu, J., Huang, P., Maggi, F., Shen, L., 2022a. Molecular investigation on CO<sub>2</sub>-CH<sub>4</sub> displacement and kerogen deformation in enhanced shale gas recovery. *Fuel* 315, 123208.
- Wu, J., Huang, P.Y., Maggi, F., Shen, L.M., 2022b. Effect of sorption-induced deformation on methane flow in kerogen slit pores. *Fuel* 325, 124886.
- Wu, J., Gan, Y., Huang, P., Shen, L., 2024. A coarse-grained approach to modeling gas transport in swelling porous media. Available at SSRN: <https://ssrn.com/abstract=4814643> or <https://doi.org/10.2139/ssrn.4814643>.
- Wu, T.H., Firoozabadi, A., 2019. Effect of microstructural flexibility on methane flow in kerogen matrix by molecular dynamics simulations. *J. Phys. Chem. C* 123 (17), 10874–10880.
- Xia, Y., Rao, Q., Hamed, A., Kane, J., Semykina, V., Zharov, I., Deo, M., Li, Z., 2022. Flow reduction in pore networks of packed silica nanoparticles: insights from mesoscopic fluid models. *Langmuir* 38 (26), 8135–8152.
- Xia, Y.D., Goral, J., Huang, H., Miskovic, I., Meakin, P., Deo, M., 2017. Many-body dissipative particle dynamics modeling of fluid flow in fine-grained nanoporous shales. *Phys. Fluids* 29 (5), 056601.
- Zeng, S., Zhang, L.Z., Zhou, J., 2021. A coarse-grained simulation of heat and mass transfer through a graphene oxide-based composite membrane. *Chem. Eng. Sci.* 243, 116692.
- Zhang, T., Javadpour, F., Yin, Y., Li, X.F., 2020. Upscaling water flow in composite nanoporous shale matrix using lattice Boltzmann method. *Water Resour. Res.* 56 (4), e2019WR026007.
- Zhao, Y.L., Wang, Z.M., Qin, X., Li, J.T., Yang, H., 2019. Stress-dependent permeability of coal fracture networks: a numerical study with Lattice Boltzmann method. *J. Petrol. Sci. Eng.* 173, 1053–1064.